





Sedimentary evidence of the Late Holocene tsunami in the Shetland Islands (UK) at Loch Flugarth, northern Mainland

MAX ENGEL , KATHARINA HESS, SUE DAWSON, TASNIM PATEL, ANDREAS KOUTSODENDRIS ,
POLINA VAKHRAMEEVA, ECKEHARD KLEMT, PHILIPP KEMPF, ISA SCHÖN AND VANESSA M. A. HEYVAERT

BOREAS


Engel, M., Hess, K., Dawson, S., Patel, T., Koutsodendris, A., Vakhrameeva, P., Klemm, E., Kempf, P., Schön, I. & Heyvaert, V. M. A. 2024 (January): Sedimentary evidence of the Late Holocene tsunami in the Shetland Islands (UK) at Loch Flugarth, northern Mainland. *Boreas*, Vol. 53, pp. 27–41. <https://doi.org/10.1111/bor.12635>. ISSN 0300-9483.

Tsunami deposits around the North Sea basin are needed to assess the long-term hazard of tsunamis. Here, we present sedimentary evidence of the youngest tsunami on the Shetland Islands from Loch Flugarth, a coastal lake on northern Mainland. Three gravity cores show organic-rich background sedimentation with many sub-centimetre-scale sand layers, reflecting recurring storm overwash and a sediment source limited to the active beach and uppermost subtidal zone. A basal 13-cm-thick sand layer, dated to 426–787 cal. a CE based on ^{14}C , ^{137}Cs and Bayesian age–depth modelling, was found in all cores. High-resolution grain-size analysis identified four normally graded or massive sublayers with inversely graded traction carpets at the base of two sublayers. A thin organic-rich ‘mud’ drape and a ‘mud’ cap cover the two uppermost sublayers, which also contain small rip-up clasts. Grain-size distributions show a difference between the basal sand layer and the coarser and better sorted storm layers above. Multivariate statistical analysis of X-ray fluorescence core scanning data also distinguishes both sand units: Zr, Fe and Ti dominate the thick basal sand, while the thin storm layers are high in K and Si. Enriched Zr and Ti in the basal sand layer, in combination with increased magnetic susceptibility, may be related to higher heavy mineral content reflecting an additional marine sediment source below the storm-wave base that is activated by a tsunami. Based on reinterpretation of chronological data from two different published sites and the chronostratigraphy of the present study, the tsunami seems to date to c. 1400 cal. a BP. Although the source of the tsunami remains unclear, the lack of evidence for this event outside of the Shetland Islands suggests that it had a local source and was smaller than the older Storegga tsunami (8.15 cal. ka BP), which affected most of the North Sea basin.

Max Engel (max.engel@uni-heidelberg.de), Heidelberg University, Institute of Geography, Im Neuenheimer Feld 348, 69120 Heidelberg, Germany and Royal Belgian Institute of Natural Sciences, Operational Directorate Earth and History of Life, Geological Survey of Belgium, Jennerstraat 10, 1000 Brussels, Belgium; Katharina Hess, Heidelberg University, Institute of Geography, Im Neuenheimer Feld 348, 69120 Heidelberg, Germany; Sue Dawson, University of Dundee, Department of Geography, Tower Building, Nethergate, Dundee DD1, UK; Tasnim Patel, Royal Belgian Institute of Natural Sciences, Operational Directorate Natural Environment, Aquatic and Terrestrial Ecology, Vautierstraat 29, 1000 Brussels, Belgium; Andreas Koutsodendris and Polina Vakhrameeva, Heidelberg University, Institute of Earth Sciences, Im Neuenheimer Feld 234, 69120 Heidelberg, Germany; Eckehard Klemm, Ravensburg-Weingarten University (RWU), Doggenriedstr., 88250 Weingarten, Germany; Philipp Kempf, Royal Belgian Institute of Natural Sciences, Operational Directorate Earth and History of Life, Geological Survey of Belgium, Jennerstraat 10, 1000 Brussels, Belgium; Isa Schön, Royal Belgian Institute of Natural Sciences, Operational Directorate Natural Environment, Aquatic and Terrestrial Ecology, Vautierstraat 29, 1000 Brussels, Belgium and University of Hasselt, Research Group Zoology, Agoralaan Building D, 3590 Diepenbeek, Belgium; Vanessa M. A. Heyvaert, Royal Belgian Institute of Natural Sciences, Operational Directorate Earth and History of Life, Geological Survey of Belgium, Jennerstraat 10, 1000 Brussels, Belgium and Ghent University, Department of Geology, Krijgslaan 281, 9000 Ghent, Belgium; received 30th March 2023, accepted 6th September 2023.

Tsunami deposits are an integral component used in the assessment of the long-term hazard of tsunami events, in particular in coastal regions with a short and fragmented historical record (Dawson & Shi 2000; Switzer & Jones 2008; González *et al.* 2009; Weiss & Bourgeois 2012; Engel *et al.* 2016). Although a range of indicative sedimentary, geochemical and micropalaeontological signatures have been established (Dawson & Shi 2000; Switzer & Jones 2008; Engel *et al.* 2016; Chagué 2020; Spiske 2020), the identification of tsunami deposits in the coastal sedimentary record poses challenges at the site scale. Tsunami deposits may vary considerably in structure and thickness depending on the hydrodynamics of the tsunami, the availability and nature of source sediments, the coastal bathymetry and topography, the depositional setting (i.e. onshore,

lacustrine, offshore) and potential post-depositional changes.

Despite an apparent scarcity of tsunamis in the shallow North Sea basin, the Shetland Islands have become an important field laboratory in which to study tsunami deposits since the early 1990s (Smith 1993; Bondevik *et al.* 2003, 2005; Dawson *et al.* 2006, 2020b; Costa *et al.* 2015; Cascalho *et al.* 2016; Buck & Bristow 2020), with summaries of the findings presented in Smith *et al.* (2004, 2019), Long (2015), Costa *et al.* (2021) and Bondevik (2022). The original studies on Shetland have played a substantial role in the advancement of tsunami sedimentology and wider tsunami geoscience. Most studies since have focused on the abundant sedimentary evidence of the tsunami triggered by the Storegga submarine slides at the

Norwegian shelf margin dated to 8175–8120 cal. a BP (Bondevik *et al.* 2012). The Storegga deposits are usually preserved in thick coastal sections of blanket peat along many of the Shetland fjords, locally called ‘voes’. They mostly consist of normally graded sand up to 40 cm thick, with large rip-up clasts, gravel components and pieces of wood embedded in the sand (Bondevik *et al.* 2003), as well as increased concentration of heavy minerals at the base (Costa *et al.* 2015; Cascalho *et al.* 2016). The deposits thin and fine inland, with sharp, in some cases erosional lower boundaries. The maximum run-up of the Storegga tsunami on the Shetland Islands is estimated to be up to 20–25 m above contemporary sea level (Bondevik *et al.* 2003, 2005; Dawson *et al.* 2020b). Deposits of the Storegga tsunami are also found in coastal lakes, consisting of normally graded coarse sand and fine gravel as well as lake-mud clasts and organic macro-remains above an erosive base. There is further evidence of a *c.* 5500 cal. a BP tsunami deposit found at Garth Loch at the east coast of Mainland (Bondevik *et al.* 2005), which was possibly also identified in western Norway (Romundset *et al.* 2015). The youngest tsunami deposit identified so far on the Shetland Islands was dated to 1500 cal. a BP and occurs as a thin inland-fining sand layer at Dury Voe (Bondevik *et al.* 2005) and Basta Voe (Dawson *et al.* 2006). Despite the solid evidence, Long (2015) considers the event ‘uncertain’ and points to possible alternative depositional processes (e.g. aeolian). The potential trigger mechanism for the late Holocene tsunami, however, is unknown (Bondevik *et al.* 2005; Dawson *et al.* 2006; Ballantyne *et al.* 2018).

Here, we present the sedimentary record of a Late Holocene high-energy flooding event from coastal Loch Flugarth, on the Shetland Islands. We discuss its origin based on a range of sedimentary criteria typically observed in tsunami deposits and the deposit’s possible relation to the other inferred tsunamis on Shetland. Our objective is to add to the palaeotsunami record on Shetland and to improve the chronology. Finally, we aim at stimulating further investigations of tsunami trigger mechanisms to improve coastal hazard assessment in the North Sea basin.

Physical setting

The Shetland Islands (1.3°W, 60.4°N) comprise a group of more than 100 islands, located at the northern margin of the North Sea, about 165 km NE of the Scottish mainland (Fig. 1A) (Mykura *et al.* 1976; Bennett *et al.* 1992). The geology of the Shetland Islands is dominated by metamorphic and metasedimentary rocks of the Caledonian Orogeny. The archipelago is tectonically divided by the major north–south running fault system of the Walls Boundary Fault (Mykura *et al.* 1976; Gillen 2003), which represents a continuation of the Great Glen Fault (GGF) (Fig. 1A). The GGF extends in

southwestern direction all the way through the Scottish mainland (Pringle 1970; Gillen 2003).

Loch Flugarth

The study site of Loch Flugarth is located in the North Roe area (northern part of Mainland; Fig. 1B) and is embedded into the Sand Voe Group, comprising thick banded hornblende and granulitic gneisses with thick lenses of amphibolite and metagabbro near the top of the Sand Voe Group (Mykura *et al.* 1976). The lake is crossed by the Flugarth Fault running from SW to NE (Pringle 1970).

The freshwater lake of Loch Flugarth covers an area of 0.16 km². It is very shallow with a maximum water depth of ~2.4 m (Murray & Pullar 1908) and no thermal stratification (Murray & Pullar 1908; Bennett *et al.* 1992). Such polymictic lakes with a non-varved record, a very simple and shallow bathymetry and limited fetch are ideal to preserve allochthonous event layers as disturbing internal processes such as hyperpycnal flows, interflows or erosion from the flanks are insignificant (Schillereff *et al.* 2014).

The lake level is ~2 m above mean sea level inside the very shallow and usually calm Sand Voe bay, from which Loch Flugarth is separated by a ~70 m wide sandy barrier (Chapelhow 1965). The barrier, which is crossed by an artificial cut, forms a flat beach with mostly sands and some gravel (Flinn 1974); its elevation is ~2 m above high tide. Stabilised aeolian dunes and till framing the beach show signs of recent erosion, whereas only the largest storm surges manage to overtop the barrier. The barrier seems to have formed inside Sand Voe bay first as a spit fed by the longshore drift, eventually forming a closed barrier. The area behind the barrier was then cut off and turned into a freshwater lake gradually filling with sediment (Flinn 1964, 1974) from organic detritus, lake-internal bioproduction, potentially aeolian input and recurring coastal overwash processes (Hess *et al.* 2023b). The only creek feeding Loch Flugarth is the Beorgs of Skelberry in the south, the organic-rich sediment input of which creates a flat, delta-type bathymetry (Murray & Pullar 1908).

Sea-level changes

Changing relative sea levels (r.s.l.) control the onshore accommodation space and sensitivity of coastal lakes to receive sediments during overwash by tsunamis or storm surges and waves (Liu 2004; Szczuciński 2020). Thus far, Holocene sea-level index points are scarce in Shetland. Based on very few dated basal peats and a limiting shell from Ronas Voe to the SW of the study site, the r.s.l. is assumed to have risen at a high rate until *c.* 7000 to 6000 cal. a BP and subsequently slowed down (Hoppe *et al.* 1965; Bondevik *et al.* 2005; Smith *et al.* 2019). For the last 1500 years, r.s.l. rise is assumed to have been

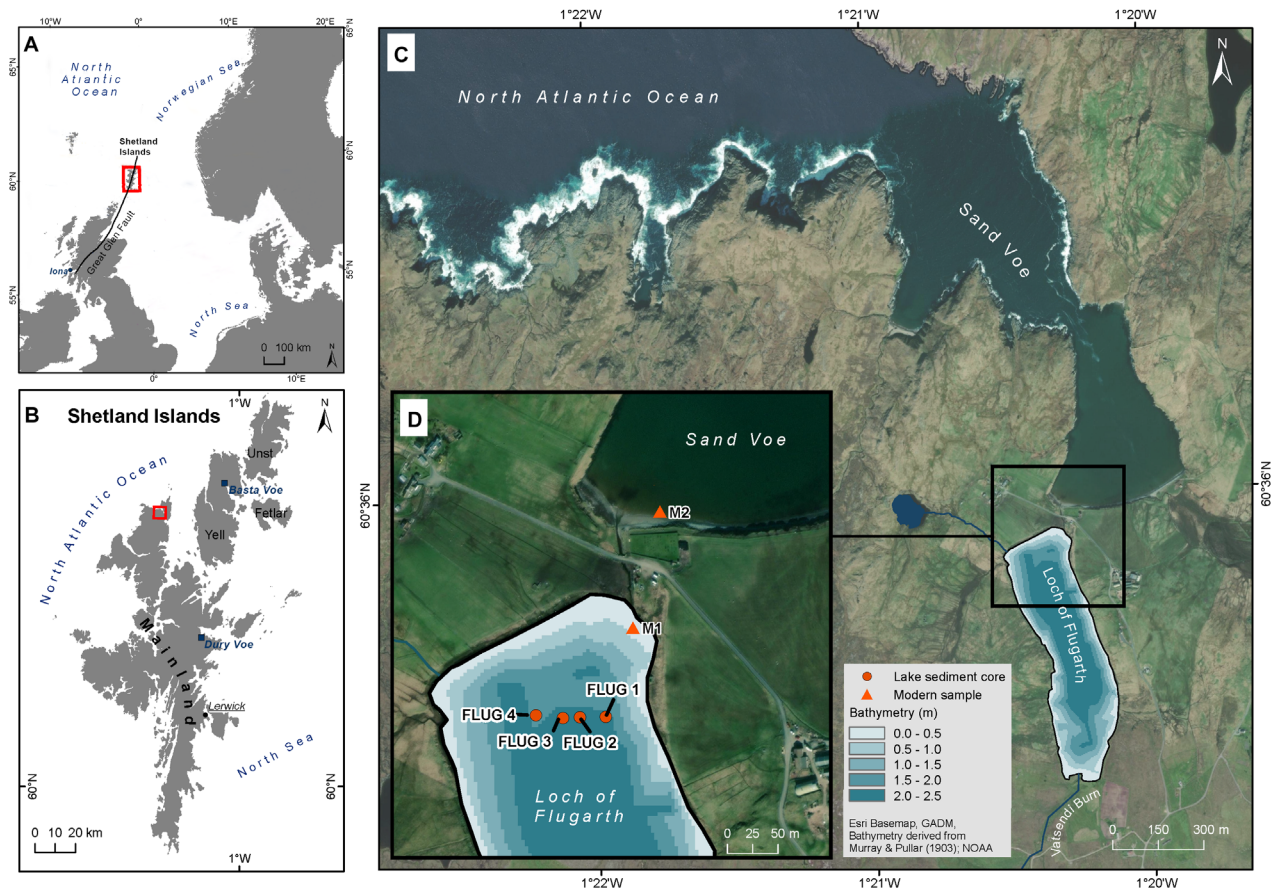


Fig. 1. The study area of Loch Flugarth. A. Location of the Shetland Islands at the border between the North Sea and the Norwegian Sea in the North Atlantic. B. Location of the Loch Flugarth in the northernmost part of Mainland. C. The setting of Loch Flugarth and Sand Voe bay, both separated by a ~2-m-high and 70-m-wide barrier. D. Location of Loch Flugarth and position of the sediment cores (FLUG 1–4), and the modern environmental samples M1 and M2.

minimal (Bondevik *et al.* 2005; Dawson *et al.* 2006) with tide gauge measurements from Lerwick showing no trend in r.s.l. since *c.* 1950 CE (Wahl *et al.* 2013). The tidal range is between 1 m (neap) and ~2 m (spring) (data from nearby Sullom Voe, Halliday 2011). Therefore, we infer a relatively stable geomorphic environment for overwash across the coastal barrier into Loch Flugarth during extreme-wave events of the last *c.* 1500 years. Under such conditions, small coastal lakes are excellent traps for tsunami deposits with good preservation potential (Kelsey *et al.* 2005; Kempf *et al.* 2017; Dawson *et al.* 2020a).

Methods

Field methods

In the central northern part of Loch Flugarth at a water depth of ~2.0 m, three sediment cores (FLUG 2–4) with lengths of up to 91.7 cm were taken at a distance of <30 m to each other using a zodiac and a UWITEC gravity corer (Figs 1D, S1, S2). They were kept in

transparent PVC liners (60 mm Ø; Fig. S2). Core FLUG 1 was taken using a Russian chamber corer that was opened at a depth of 200 cm below the lake bottom to generate an undisturbed stratigraphic sample at a core depth of 200–250 cm (Fig. S4). Additionally, two surface samples of modern sedimentary environments were taken to identify sediment sources. In this study, we focus on the basal part of cores FLUG 2 and 3. The upper parts of these cores were analysed for storm overwash by Hess *et al.* (2023b).

Sedimentary analyses

After splitting and describing the cores at the laboratory of the Geological Survey of Belgium at Brussels, a Geotek multi-sensor core logger was used at the Renard Centre of Marine Geology, Ghent University, Belgium. High-resolution photographs were taken using the Geoscan IV line-scan camera. Bulk density (γ -ray attenuation densometer) and magnetic susceptibility (Bartington point sensor MS2E) were measured in steps of 2 mm.

X-ray computer tomography (CT) scans were generated at Ghent University Hospital using a Siemens Somatom Definition Flash Medical X-ray CT scanner. The voxel sizes of the image stacks are $0.15 \times 0.15 \times 0.3$ mm. The stacked core images were analysed qualitatively using the Fiji software package (Schindelin *et al.* 2012).

For grain-size analysis of the bottom sand unit in FLUG 3, a Fritsch Analysette 22 NeXT Nano laser diffractometer with a measurable range of 0.1–3800 μm was used at the Laboratory for Geomorphology and Geoecology, Heidelberg University, Germany. The thickness of each sample was 2 mm – one-fifth of what is recommended for tsunami deposits (Spiske 2020). Samples were dried at 105 °C and carefully pestled. Organic matter was dissolved by adding H_2O_2 (30%). Aggregates were dispersed using 0.1 mol $\text{Na}_4\text{P}_2\text{O}_7$ (44.6 g L^{-1}). GRADISTAT v9.1 (Blott & Pye 2001) was used to calculate univariate statistical measures following Folk & Ward (1957).

Elemental concentrations were measured with an Avaatech (GEN-4) X-ray fluorescence core scanner at the Institute of Earth Sciences, Heidelberg University. The core scanner uses an OXFORD ‘Neptune 5200’ series 100 W X-ray source with a Rh anode. The slit size was 5.0 mm down-core and 10.0 mm cross-core. Two different energy levels were applied for measurement: at 10 kV with a current of 500 μA without a filter and a dwell time of 10 s, and at 30 kV beam with a 1500 μA current, a Pd-thick filter and dwell time of 10 s. The data were processed using the bAxil software (Brightspec 2015). The elements were normalised by dividing the intensity counts of each element by the X-ray fluorescence total during each run excluding coherent and incoherent scattering (Kern *et al.* 2019).

Principal component analysis (PCA) was first carried out on 13 centred log-ratio transformed elements (Al, Br, Ca, Fe, K, Mn, Mo, P, Rb, S, Si, Sr and Zr) and subsequently on indicative element ratios. The first five principal components (PCs) from the second PCA were used for the hierarchical clustering of principal components (HCPC) to identify the most significant variables and to identify potential differences between types of sand layers in the cores. The PCA and the HCPC were performed in R studio (Kassambara 2017) by applying the R packages FactoMineR (v2.4) for computing and factoextra (v1.0.7) for visualisation. Significance tests were applied to analyse whether the differences between the clusters are statistically significant. A Kruskal–Wallis test (R package vegan v2.5-7) and a Dunn’s post-hoc test (R package dunn.test v1.3.5) identified characteristic variables controlling the clusters. The output resulted in Bonferroni-corrected p -values with $\alpha > 0.05$.

A total of nine samples from selected core depths representing the different facies were processed for palynological analysis following standard techniques, including: freeze-drying, weighing (range of sample dry

weights 0.1–0.7 g), spiking with *Lycopodium* spores (batch no. 050220211), treatment with HCl, NaOH and HF, heavy liquid separation, sieving (10 μm) and mounting of the residues on glass slides using glycerin jelly. All samples were screened to identify the most common palynomorphs.

Chronology

A combination of ^{14}C and ^{137}Cs dating was used to establish a Bayesian age–depth model for the entire stratigraphy of FLUG 2 and 3. Samples for ^{14}C dating were measured by accelerator mass spectrometry at the Poznań Radiocarbon Laboratory, Poland (Goslar *et al.* 2004). Calibration of the ^{14}C data was carried out using the IntCal20 data set (Reimer *et al.* 2020). Details on ^{137}Cs dating are compiled in Data S1. For Bayesian age–depth modelling rBacon (Blaauw & Christen 2011) was applied. Variable sedimentation rates or event layers were considered in the model according to Blaauw & Christen (2011) (Table S2). Late Holocene ^{14}C dates of tsunami stratigraphies in the Shetland Islands presented in Bondevik *et al.* (2005) were recalibrated using Calib software (v8.2) (Stuiver & Reimer 1993) and the IntCal20 data set (Reimer *et al.* 2020) (Table S3). Data on the bulk density, X-ray fluorescence and CT scans and the age–depth model were first published in Hess *et al.* (2023b).

Results

Facies description

Visually, four different facies types were identified in cores FLUG 2 and 3 (Table 1, Fig. 2). The organic-rich facies 1–3 are distributed across the entire stratigraphy in varying thicknesses, and are interspersed with 40 thin, sub-centimetre-scale layers of facies 4 (light sand with sharp upper and lower boundaries, L1–L40 in Fig. 2). These sand layers enable unequivocal correlation between FLUG 2 and 3. Facies 1 (dark-brown muddy peat, with diatom fragments) dominates the upper 35 cm in FLUG 3, while facies 3 (organic-rich, brown mud with a minor sand component) is more prevalent between 35 and 73 cm in FLUG 3. Facies 2 (organic-rich, light-brown mud) occurs at 40–45 cm and 73–77 cm b.s. (below sediment surface) in FLUG 3 (Fig. 2). At the base of the cores, a thick section of facies 4 was found (78.5–91.7 cm b.s. in core FLUG 3; 69.0–77.0 cm b.s. in core FLUG 2) (Fig. 2). More details on the complete lithostratigraphy can be found in Hess *et al.* (2023b).

The modern surface samples representing potential source environments for *ex-situ* deposits inside the lake were taken from the foot of the barrier at the lake margin (FLUG-M1) and from the wet beach (FLUG-M2) (Fig. 1D). Both are very similar, consist of pure, relatively well-sorted sand and can be considered representative of the major part of the barrier complex.

Table 1. Facies classification of layers in cores FLUG 2 and 3 based on visual classification and multivariate statistical analyses (principal component analysis (PCA), hierarchical clustering of principal components (HCPC)), and the correlation of both schemes. A brief interpretation of depositional processes is provided for each cluster.

Visual classification		PCA and HCPC		Process interpretation
Facies	Description	Cluster	Description	
Facies 1	Dark-brown muddy peat, with diatom fragments	Cluster 4 (red)	Muddy peat	Internal lake sedimentation with fluvial input of peat from the catchment
Facies 2	Organic-rich, light-brown mud	Cluster 3 (grey)	Organic-rich mud with sand	Internal lake sedimentation with minor fluvial input of peat from the catchment and a very minor aeolian component
Facies 3	Organic-rich, brown mud with a minor sand component			
Facies 4	Pale-yellow sand of varying thickness	Cluster 2 (yellow)	Thin sand layers	Storm overwash
		Cluster 1 (blue)	Thick basal sand	Tsunami deposition

The thick basal sand and the remaining 40 thin sand layers above, which were identified based on the CT scans (Fig. 2), share a similar sand source. However, the multi-proxy data reveal differences that go beyond the mere thickness. Compared with the thin sand layers above, the basal sand is finer and less sorted, and free of carbonate, and the pore space is partially filled by a mud matrix.

The magnetic susceptibility is highest in the basal sand, much higher than in the thinner sand layers. Elemental ratios of Sr/Br (Fig. S3) and Zr/K reach maximum values in the basal sand section and are up to almost an order of magnitude higher than in the thin sand layers above. In contrast, S/Ti values, which peak in facies 1 (muddy peat), are lowest in the basal sand, much lower than in the thin sand layers L1–L40 (Fig. 2).

These differences are corroborated by the PCA and the HCPC. Initially, element counts were used for the PCA. The first two PCs explain 47.2% (PC1) and 14.0% (PC2) of the variance of the whole data set, respectively (Fig. S5). PC1 is driven by the variance of Al, Br, K, Rb, S, Si and Zr, whereas PC2 is mainly driven by Ti. These results were used to establish ratios with conservative elements (e.g. Ti, Fe, Si, K) as the denominator, mostly Ti as it is neither contributed by internal biogenic processes nor influenced by redox conditions or diagenetic overprinting (Chagué 2020). The PCA on ratios shows four separate clusters and a clear distinction of the basal sand (cluster 1) from the remaining sand layers (cluster 2) and the organic-rich background facies (clusters 3 and 4) (Fig. S6). While the basal sand shows high ratios of Zr/K, Sr/Br and Zr/Rb, the thin sand layers show high ratios of K/Ti, Si/Zr and Si/Ti. The HCPC based on the eigenvalues reveals five dimensions and also

four clusters, very similar to those of the PCA. The sands of facies 4 are again clearly separated into clusters 1 and 2 (Fig. 3, Table 1) with Zr/K and Sr/Br showing the strongest significance for the basal sands (cluster 1). In contrast, the upper thin sand layers (cluster 2) are mostly driven by Si/Ti and K/Ti (Fig. 4).

An initial screening of pollen content across core FLUG 3 also revealed differences between the basal sand and the remaining core: the seven samples between 3 and 73 cm b.s. are all rich in terrestrial pollen and spores. They are dominated by Ericaceae (heath), Poaceae (grasses) and Cyperaceae (sedges) pollen representing the heath and grasslands around Loch Flugarth. These samples also contain various pollen grains from herbs and fern spores, as well as sporadic arboreal pollen such as *Betula* (birch), *Alnus* (alder), *Pinus* (pine) and *Salix* (willow). In contrast, the two samples from the basal sand (81 and 86 cm b.s.) contain only very few reworked pollen grains of poor preservation.

Sublayers of the basal sand

The grain-size analysis allows for an internal differentiation of the basal sand into four sublayers (Fig. 5). From bottom to top, sublayer 1 (91.7–88.5 cm b.s.) has a lower section of unimodal, moderately to poorly sorted massive sand, and highest values of Zr/K and bulk density. The upper part is normally graded, shifting to bimodal (sand and minor silt component) and trimodal (sand and minor silt and clay components) grain-size distributions (Fig. 7), which are very poorly to extremely poorly sorted. The Zr/K values and bulk density decrease in the upper part.

Sublayer 2 (88.5–82.7 cm b.s.) has a lower inversely graded section changing from a mixture of sand and silt to pure sand, with better sorting towards the top and slightly increasing bulk density as well as stable magnetic susceptibility and Zr/K values. The upper part is again normally graded with a distinct change from silty sand to sandy silt at 83.9 cm b.s. and the highest values for magnetic susceptibility of the entire succession. The uppermost part of sublayer 2 is less sorted and shows a decrease in Zr/K and an initial doubling of S/Ti ratios. This might be associated with millimetre-scale muddy peat clasts embedded in the silty to sandy matrix, the largest of which is >1 cm in vertical extent (Figs 5, S8).

There is a sharp contact to sublayer 3 (82.7–80.6 cm b.s.) with a very thin inversely graded base followed by a normally graded top section with increasing concentration of organic matter and small mud clasts. The Zr/K decreases in the entire sublayer, along with bulk density and magnetic susceptibility, while the S/Ti levels remain elevated.

Sublayer 4 (80.6–78.6 cm b.s.) of massive sand has an erosive lower boundary, elevated S/Ti values and millimetre-scale muddy peat clasts. It shows a distinct peak in magnetic susceptibility and bulk density

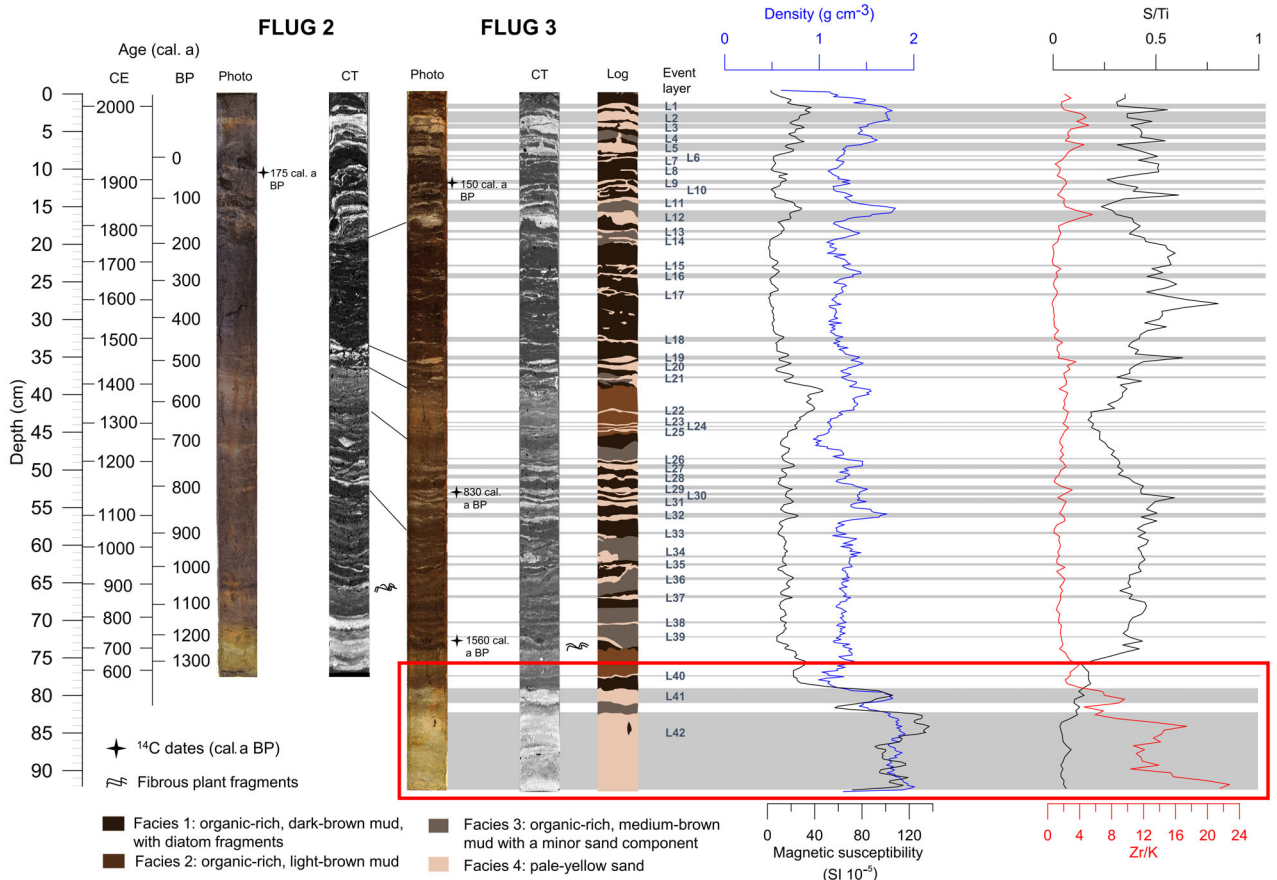


Fig. 2. Overview of the lithostratigraphy. From left to right: light photograph and computer tomography (CT) scan of FLUG 2; light photograph, CT scan and facies distribution of FLUG 3, including key correlation layers with FLUG 2; high-resolution data of bulk density and magnetic susceptibility; S/Ti and Zr/K ratios (modified from Hess *et al.* 2023b). The red box indicates the core section shown in Fig. 5.

associated with a weak increase in Zr/K values, and is better sorted than sublayer 3. Its upper boundary to facies 3 is sharp, where Br/Ti (Fig. S3) and S/Ti rise strongly, while the magnetic susceptibility, bulk density and Zr/K values decrease (Fig. 5).

Age of the basal sand

Age–depth modelling based on ^{14}C and ^{137}Cs reveals a chronostratigraphy of *c.* 1450 years. The four ^{137}Cs dates (see age model in Data S1) and the surface date were integrated together with the ^{14}C data into the main age–depth model for the entire core. Two outliers (FLUG 3-30-31 and FLUG 3 14C-4; Fig. 6, Table 2) both creating significant age inversions in the stratigraphy were not considered for further analyses. After removing all depositional events (in total 19 sand layers, $L \geq 2$ mm; Table S2) by identifying their upper and lower boundaries in the age–depth model and subsequent reintegration at their real depth (cf. Sabatier *et al.* 2022), the basal sand layer reveals an age of 426–787 (2σ ; median: 569) cal. a CE. Considering a 1σ -error, the age span reduces to 536–701 (median 594) cal. a CE. The averaged

accumulation rate across the entire core is 20 cm^{-1} (Fig. 6). Further details on the construction of the age model can be found in Data S1.

Discussion

Sediment sources

The three types of organic-rich facies mainly represent lake-internal sedimentation with a contribution of organic matter through surface discharge from the peat-bog catchment. The highest Br and S in facies 1 (cluster 4), which are best preserved in fine-grained organic matter (Engel *et al.* 2012; Chagué 2020; Biguenet *et al.* 2021), may indicate increased rainfall and surface discharge (McIlvenny *et al.* 2013). The sand component in facies 3 (cluster 3) might relate to phases of higher aeolian sand input from the sand barrier of Sand Voe, a process that has been identified in several coastal lakes and peat bogs in the UK (e.g. Swindles *et al.* 2018; Kylander *et al.* 2020).

The thin sand layers of facies 4 (L1–L40) have been interpreted as deposits of individual overwash events

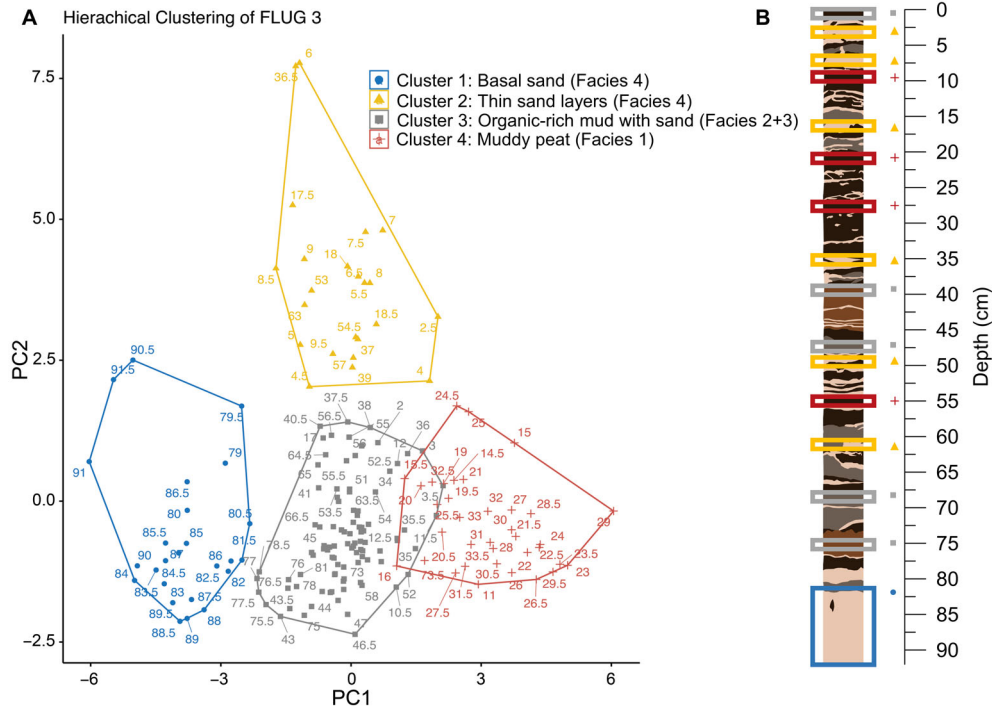


Fig. 3. A. Factor map showing the results of the hierarchical clustering of principal components (HCPC) with four different clusters and 95% confidence intervals. Numbers indicate the depth of a measurement in cm b.s. (below sediment surface). B. Core FLUG 3 indicating the origin of exemplary samples shown in the HCPC. Colours of the frames refer to colours of the grouping in the HCPC plot (modified after Hess *et al.* 2023b). PC1 is mainly driven by Br/Ti and S/Ti and, thus, by organic matter. It inversely correlates with heavy mineral content. This may be a function of sediment source from distal (shallow marine to coastal) with low values to increasingly proximal (beach → catchment → internal bioproduction). PC2 is mainly driven by Si/Ti and Si/Zr (Fig. S6), reflecting the beach (and dune) sand.

originating from the dune, beach and uppermost subtidal area of Sand Voe during major storm events. This interpretation is mostly based on their similarity with local beach sands, sharp upper and lower contacts and occasional gravel components (Hess *et al.* 2023b). The combination of tides, storm surge and wave run-up exceeding the threshold height of the barrier displace sand from the beach and the barrier and wash it into the coastal lake. They may create washover fans proximal to the barrier, mainly through bedload sedimentation, which extend to thin centimetre- to millimetre-scale sand sheets inside the coastal lake (Liu 2004; Chaumillon *et al.* 2017). The sediment source area for the thin sand layers is confirmed by the large overlap of endmember 1 of the endmember modelling analysis of grain-size distributions of the entire core by Hess *et al.* (2023b). Endmember 1 represents the thin layers of sandy storm deposits and fully overlaps with the grain-size distribution of the modern beach sand and the subaerial backside of the barrier (Fig. 7). Endmember modelling decomposes grain-size distributions of a data set by calculating a low number of synthetic distributions best representing the variability of the data set. This helps to distinguish and group similar distributions and to unmix and quantify different sediment sources represented in individual samples (Dietze & Dietze 2019).

Facies 4 is separated into two distinct clusters, i.e. the thin storm sand layers and the thick basal sand layer. The basal sand is dominated by high values of Zr/K, Fe/Ti and Sr/Rb. Zr/K most likely reflecting the concentration of zircon as one of the highest-density minerals (Davies *et al.* 2015), which, despite generally low percentages, has been shown to be enriched in tsunami deposits (Costa *et al.* 2015; Chagué 2020). Zircon grains require high-energy flows to generate sufficient shear stress to become mobilised (Cuven *et al.* 2013). Furthermore, the very low S/Ti ratio (Fig. 4) may be driven by high Ti concentrations associated with heavy mineral content (cf. Cuven *et al.* 2013; Chagué 2020). In contrast, the storm deposits are dominated by K and Si, i.e. mainly quartz and feldspar varieties (Chagué 2020) as in the beach sand. This is confirmed by the HCPC (Fig. 3) as well as the Kruskal–Wallis test and Dunn’s post-hoc test (Fig. 4).

Evidence for tsunamigenic origin of the basal sand

The basal sand stands out against the background sediments in terms of bulk density and magnetic susceptibility, which is caused by high-density ferromagnetic iron oxides or heavy minerals, and is a typical signature of tsunami deposits in lakes (Wagner *et al.* 2007; Kempf *et al.* 2017). Suspension grading,

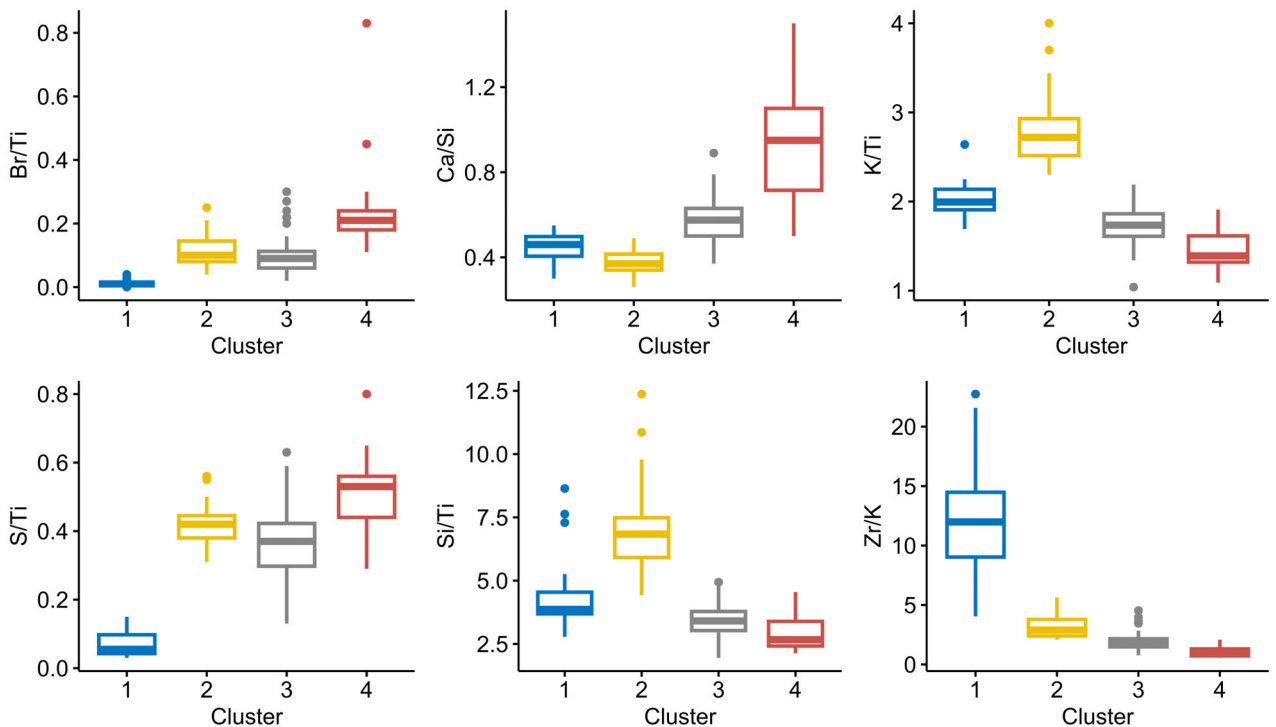


Fig. 4. Boxplots showing the significance of the six most important ratios for each cluster with Bonferroni-corrected p -values. Values on the y -axis indicate how much the four different clusters of the hierarchical clustering of principal components (HCPC) analysis are driven by these individual element ratios. Colours and numbers of clusters are the same as in Fig. 3.

which is observed in sublayers 1–3 (Fig. 5), is a common sequential pattern in tsunami deposits (Bondevik *et al.* 1997; Dawson & Shi 2000). It forms when a tsunami loaded with suspended sediment impacts a coastal lake or a coastal plain still inundated from the previous wave. Grains settle as a function of their size, shape and density under Stoke's law of hydraulic equivalents, with smaller and lighter particles increasing towards the top (Dawson & Shi 2000; Spiske 2020). Therefore, the heavy mineral content, in the current case reflected by Zr/K, tends to be higher in the lower parts of sublayers that are only partially formed by suspension grading (cf. Bahlburg & Weiss 2007; Moore *et al.* 2011; Cascalho *et al.* 2016; Spiske 2020). The increased heavy mineral content in combination with the bi- to trimodal pattern of finer sand grains and mud in samples from the upper part of the normally graded sublayers (Figs 5, 7) indicates a larger source area than the thin sand layers above. This source area probably comprises the dune, the beach, Sand Voe bay and marine areas outside of Sand Voe bay, at water depths out of reach for storm waves. This pattern of the source area is typical of tsunami deposits when compared with storm deposits (Switzer & Jones 2008; Engel *et al.* 2016; Spiske 2020).

In between sublayers, sharp and undulating erosional boundaries are common (Coven *et al.* 2013; Spiske 2020), such as at the base of sublayers 3 and 4 (Fig. 5). Tsunamis erode underlying fine-grained and/or organic-rich substrate onshore during both run-up and backwash. The

cohesive clasts become entrained in the turbulent flow and embedded into the sandy tsunami deposit as rip-up clasts (Coven *et al.* 2013; Spiske 2020), which have been reported from tsunami deposits in various coastal lake archives (Bondevik *et al.* 1997; Kelsey *et al.* 2005; Wagner *et al.* 2007; Kempf *et al.* 2015, 2017).

Sublayer 2 shows a distinct inversely graded section, which may relate to the process of kinetic sieving where grain–grain collisions in the basal part of the flow cause finer particles to trickle down and settle before the larger particles (Sohn 1997). Such traction carpets indicate high shear stress from the suspension-laden flow and have been identified in several tsunami deposits (Moore *et al.* 2011; Falvard & Paris 2017). However, an upward reduction in bulk density with increasingly coarser particles as observed by Moore *et al.* (2011) is not reflected by the present data.

A distinct mud cap on top of the entire tsunami succession, such as observed in an organic-poor, gyttja-type lake (Kempf *et al.* 2015, 2017) or clay-rich marsh deposit (Coven *et al.* 2013), cannot unequivocally be inferred from the photographs and CT scans (Fig. 2). However, there is an increasing concentration of finer particles and organic matter in the upper part of sublayer 3, possibly reflecting the waning stage between two waves, a pattern that has been found in other tsunami deposits of shallow coastal lakes as well (Bondevik *et al.* 1997; Bondevik 2022). The low concentration and poor preservation of pollen in the basal sand compared

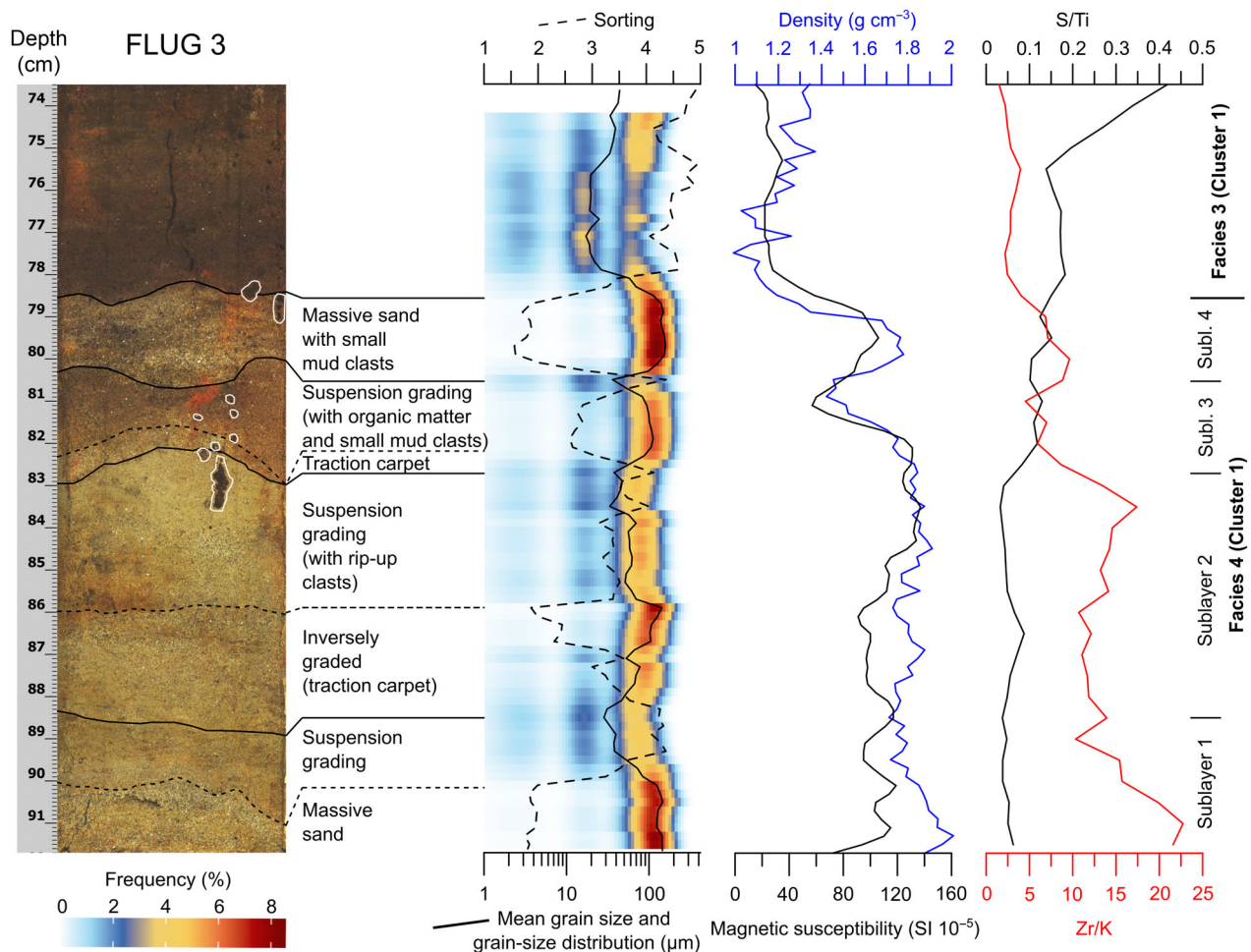


Fig. 5. Core photograph of the basal sand section with sublayers and small peat clasts marked by thin white outlines. The sublayers are shown with mean grain size, sorting, grain-size distribution, magnetic susceptibility (from the present study), bulk density, S/Ti and Zr/K (Hess *et al.* 2023b).

with all other facies of the core are in agreement with observations from tsunami deposits in the region (Smith *et al.* 2004) and elsewhere (Chagué-Goff *et al.* 2012).

The characteristics of the basal sand section overlap with typical criteria of tsunami erosion and deposition in the proximal coastal lake environment *sensu* Kempf *et al.* (2017). Alternative mechanisms can be excluded, as we can clearly distinguish them from the site-specific pattern of the overlying storm deposits, while the sorting is too poor for aeolian input. Furthermore, we exclude major changes to the geomorphic framework of the sedimentary archive of Loch Flugarth, as r.s.l., which is the most crucial controlling factor, is assumed to have not changed notably during the last 1500 years (Dawson *et al.* 2020b).

The investigated gravity cores may not reach the base of the candidate tsunami deposit. However, this affects neither the interpretation presented above nor the chronological estimates discussed in the following section. The finding of brownish organic-rich (comparable to facies 1–3) layers and some greyish, more

minerogenic layers at a depth of 250–200 cm below the lake bottom in FLUG 1 (Fig. S4) shows that the record may extend beyond the Late Holocene. Prior work at the site indicates two distinctive units deeper down in the record possibly corroborating with earlier high-energy inundation to the lake basin (Sue Dawson, unpubl. data). Thus, using more advanced coring techniques, a more complete Holocene record and additional event deposits may be accessed and investigated at Loch Flugarth.

Timing and trigger of the tsunami

The age range for the basal sand of 426–787 cal. a CE or 1524–1163 cal. a BP, respectively (536–701 cal. a CE or 1414–1249 cal. a BP with 1σ error), is based on the age–depth model and considered to represent the time window in which the inferred tsunami occurred. Age overestimation owing to excessive reworking of the ^{14}C -dated material used for the age–depth model is assumed to be negligible, as outliers were manually

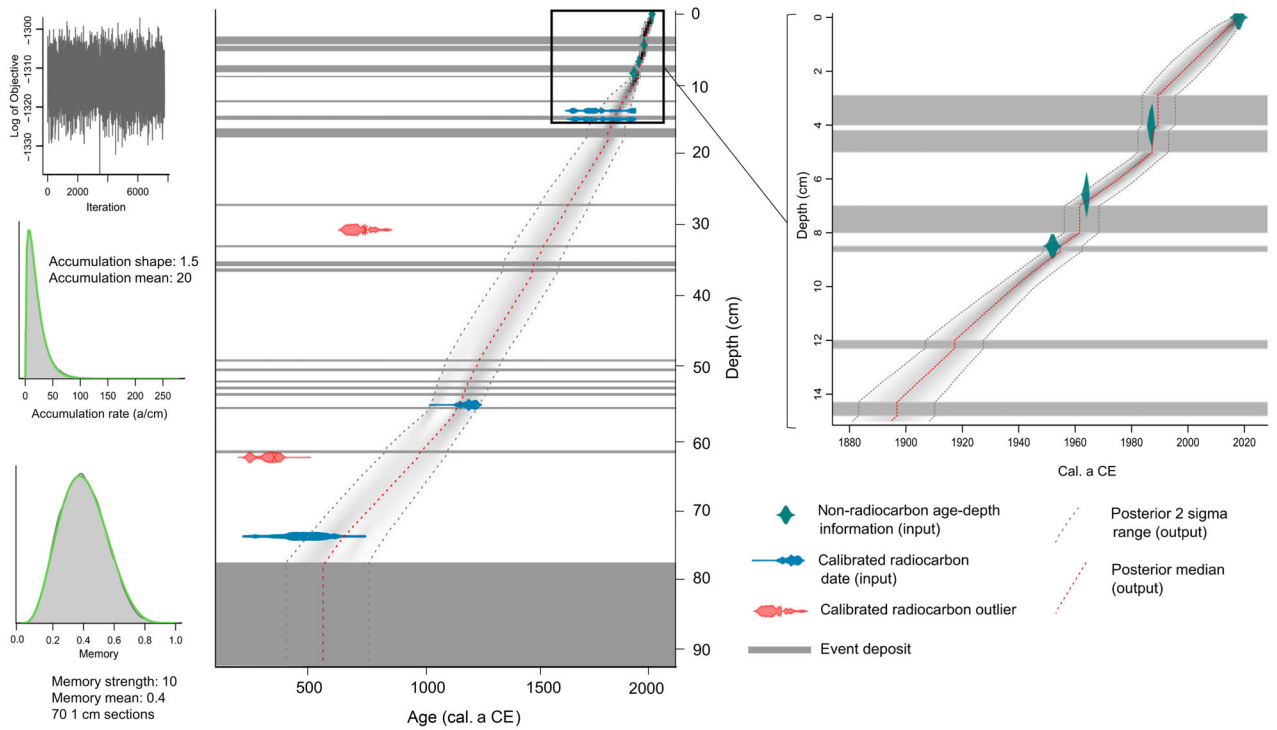


Fig. 6. rBacon-based age–depth model based on radiocarbon data (blue) and ^{137}Cs data (green). The posterior age–depth model with the median (red dashed line) and the 2σ error range runs from bottom left to top right. The horizontal bars in the figure represent the event deposits >2 mm thick (modified after Hess *et al.* 2023b).

eliminated before running the age–depth model (Data S1, Fig. 6, Table 2) (Hess *et al.* 2023b).

There are tsunami deposits found at two locations on the Shetland Islands which overlap with this time range. At Dury Voe, east Mainland, a thin sand layer located within thick coastal peat was traced in outcrops from the inner fjord up to some 400 m inland and up to an elevation of 5.6 m above high tide. Two ^{14}C dates were retrieved 7–8 cm (2303–1927 cal. a BP) and 1–2 cm (1818–1520 cal. a BP) below the sand layer. One ^{14}C dating was generated 1–2 cm above the sand layer (1507–1287 cal. a BP) (Table S3) (Bondevik *et al.* 2005). These data are maximum ages as the dated objects could have been subject to some limited reworking. Also, the lower

ages pre-date the event by an unknown amount of time as it is unclear how much of the peat stratigraphy was eroded by the tsunami. The location is proximal to the shoreline where shear stress by tsunami flow may still have been high. We argue that the maximum age generated right on top of the sand layer is more indicative for the timing of the Dury Voe tsunami event and may suggest an age younger than the 1500 cal. a BP estimated by Bondevik *et al.* (2005).

At the inlet of Basta Voe, northeast coast of Yell, three thin sand layers were identified in peat outcrops close to the coast, the uppermost of which continuously extends for ~ 2 km inland (Dawson *et al.* 2006). It can also be traced in ground-penetrating radar measurements (Buck

Table 2. ^{14}C data of samples from Loch Flugarth (Hess *et al.* 2023b). Calibrated ages with an asterisk indicate deposition after 1950 CE. Those in brackets were interpreted as outliers (too old) and not considered for the age–depth model. ^{14}C data were calibrated using the IntCal20 data set (Reimer *et al.* 2020). b.s. = below lake bottom.

Sample ID	Lab. no. Poz-	Material	Depth (cm b.s.)	$\delta^{13}\text{C}$	^{14}C age (a BP)	Error	Age (cal. a CE, 2σ)	Age (cal. a BP, 2σ)
FLUG 2 ^{14}C -1	123190	Plant remains	10.5	−25.4	175	± 30	1658–1950*	Modern
FLUG 3-16 ^{14}C	127787	Plant remains	14.7	−34.0	150	± 30	1667–1950*	Modern
FLUG 3-30-31	138860	Organic-rich sediment	30.5	−32.9	1265	± 30	(666–775)	(1284–1175)
FLUG 3 ^{14}C -3	123189	Plant remains	55.5	−31.1	830	± 30	1167–1267	783–683
FLUG 3 ^{14}C -4	123187	Plant remains	63.0	−37.1	1710	± 35	(250–416)	(1700–1534)
FLUG 3-80 ^{14}C	127788	Plant remains	74.0	−49.0	1560	± 90	261–651	1689–1299

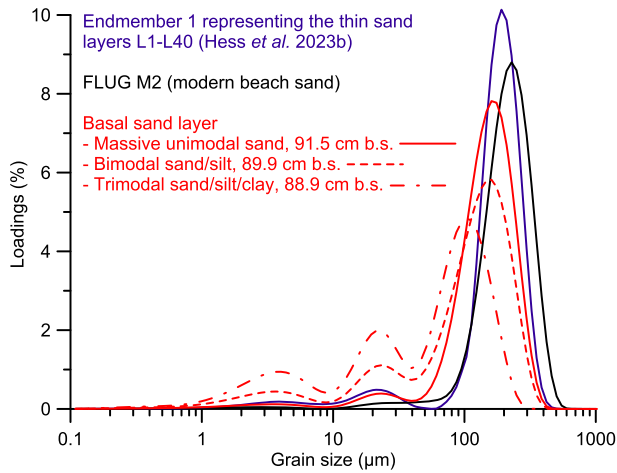


Fig. 7. Grain-size distributions of the modern beach at Flugarth, and three representative samples showing the range of distributions within one normally graded sublayer of the basal sand layer (cluster 1/facies 4, red lines). Additionally, the distribution of endmember 1 of the endmember modelling analysis in Hess *et al.* (2023b), representing the thin sand layers from storm overwash above the basal sand is shown for comparison.

& Bristow 2020). The sand layer is bracketed by two overlapping ^{14}C dates: 0–1 cm below the sand layer, 1546–1345 cal. a BP; 5 cm above the sand layer, 1517–1303 cal. a BP (Table S3) (Bondevik *et al.* 2005; Dawson *et al.* 2006). Based on the overlap, the age range probably

covers the event. Chronological data from both sites point to an age of the tsunami around 1400 cal. a BP (or even younger) rather than 1500 cal. a BP, considering that reworking of dated material may also have played a role. This chronological estimate is in accordance with the chronological interpretation of the basal sand in FLUG 2 and 3 (Fig. 8), which possibly represents the Dury Voe tsunami *sensu* Bondevik *et al.* (2005).

A source for the Dury Voe tsunami has not yet been identified. A local coastal or submarine landslide has been discussed (Bondevik *et al.* 2005; Dawson *et al.* 2006; Ballantyne *et al.* 2018), but without any physical evidence from seafloor mapping (Long 2015). Based on their limited size, none of the post-Storegga slides known north of the Shetlands seems capable of triggering a tsunami (Haflidason *et al.* 2005; Smith *et al.* 2019).

Comparison with the historical record of tsunamis

Recently, Mac Conamhna (2023) reported the possible observation of a tsunami in the earliest written chronicles of the Gaelic world. The chronicle entry from the monastery of Iona in the Outer Hebrides, passed on in three different Medieval annals (*Chronicum Scotorum*, the Annals of Tigernach and the Annals of Ulster), mentions ‘A belch/bursting forth/huge tidal wave/eruption of the sea in the month of October’ (Mac Conamhna 2023). Furthermore, the Annals of Ulster

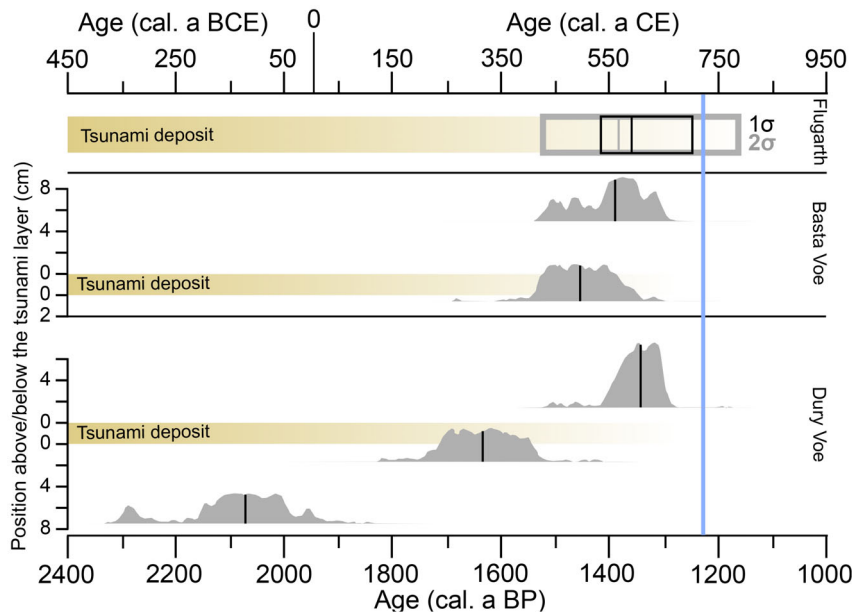


Fig. 8. Timeline showing recalibrated ^{14}C data above and below the tsunami deposits of Dury Voe and Basta Voe (Table S3; Bondevik *et al.* 2005) in combination with the age of the candidate tsunami deposit from Loch Flugarth based on the age–depth model of the present study (Data S1, Fig. 6). Grey curves show the probability distributions, and black or grey vertical lines show the median age. The grey box for Loch Flugarth indicates the maximum and minimum age based on the 2σ error. The black box indicates the age interval based on the 1σ error. The light blue bar indicates the timing of the assumed seismic tsunami recorded in the Irish annals (Mac Conamhna 2023). The base of the curves refers to the vertical position of the dated sample in reference to the tsunami deposit. ^{14}C dates below the deposits represent maximum ages with an uncertain time gap. ^{14}C dates above the deposits represent minimum ages of the tsunami deposit under the assumption that the dated organic material was embedded into the stratigraphy immediately after death and corresponds to the age of the surrounding deposit.

contain the record of ‘An earthquake in October’. Both events are ascribed to the year 720 CE, indicating a major seismic event triggering a tsunami that impacted the Outer Hebrides and potentially other coastal regions of the northern British Isles. Mac Conamhna (2023) associates this event with seismicity along the GGF running across the Scottish mainland from the southern Hebrides up to the Shetland Islands in a SW–NE direction, and draws a correlation with the deposits of the Dury Voe tsunami on Shetland. However, Fig. 8 shows that maximum ages for the event beds at Dury Voe, Basta Voe and Loch Flugarth appear too old. There is a small overlap with the age range of the Flugarth deposit from this study, although the 720 CE archive entry is more than 160 (2σ error) or 126 (1σ error) years younger than the median age from Flugarth. A correlation can only be established under the assumption that the dated objects at all three sites are systematically older than their sedimentary contexts, which is considered unlikely.

There are diverging conclusions on the earthquake record of the GGF (Musson 2007; Piccardi 2014), which is mostly driven by glacio-isostatic rebound (Davenport *et al.* 1989; Ringrose 1989). The two strongest historical earthquakes on Scottish territory with proper documentation, both of which could be associated with the GGF, have estimated magnitudes of 5 (1901 CE) and 5.1 (1816 CE), respectively (Piccardi 2014), with no reported tsunamis. Onshore palaeoseismological data indicate maximum possible magnitudes of 6.0–7.5 following deglaciation (13 000–6000 cal. a BP) and of 6.5 afterwards (Davenport *et al.* 1989). Based on these data, it is highly speculative whether a submarine segment of the GGF had the ability to generate a major earthquake and tsunami that impacted coastal sections spanning from the Outer Hebrides up to the Shetland Islands and generate a tsunami bed at several sites with both northern and eastern exposure across the Shetland archipelago. Thus, the trigger mechanisms of the Dury Voe tsunami and the seismic and coastal flooding event recorded near Iona still remain elusive based on the few existing records.

Conclusions

Sediment cores from Loch Flugarth on northern Mainland, Shetland Islands, show a clear separation between organic-rich mud of varying composition and thin allochthonous sand layers. The allochthonous sand occurs in thin sub-centimetre layers throughout the core and results from storm overwash. These thin layers differ from the thick basal sand in all cores in terms of grain-size distribution, sediment structure and chemical composition. High values of Zr/K and magnetic susceptibility as well as low S/Ti values point to enriched heavy minerals. Poorer sorting, partially with bi- and trimodality, as well as suspension grading in sublayers, some of them also showing traction carpets and rip-up clasts, indicate

deposition by a tsunami. The age–depth model and correlation with tsunami deposits of similar age in the Shetland Islands suggests an age around 1400 cal. a BP (*c.* 536–701 cal. a CE; 1σ error). Correlation with a historical, allegedly seismic tsunami observed on the Outer Hebrides in 720 CE seems questionable based on the chronological evidence.

While the present study adds to the growing evidence of the Late Holocene Dury Voe tsunami, it prompts the need for further research on the spatial distribution and impact of tsunamis in the North Sea region, and the possible triggers as a basis for future hazard assessment. From a more local perspective, this study corroborates the assumption that the site represents an archive of event deposits beyond the last 1500 years. Loch Flugarth preserves both tsunami and storm deposits that can be unequivocally distinguished based on sedimentological and geochemical criteria. Therefore, we advocate for exploration of the deeper sediment record of Loch Flugarth to improve our chronological estimate and correlation of the Dury Voe tsunami and possibly other regional tsunamis such as the Garth tsunami (*c.* 5500 cal. a BP) and to also extend the palaeotempestological record of the northern North Sea.

Acknowledgements. – This study was kindly funded by Belgian Science Policy Belspo (BR/175/PI/GEN-EX). For the publication fee we acknowledge financial support by Deutsche Forschungsgemeinschaft within the funding programme ‘Open Access Publikationskosten’ as well as by Heidelberg University. The possibility for Geotek core logging at Renard Center of Marine Geology, Ghent University, and the support by Evelien Boes are acknowledged. The permission to access Loch Flugarth was kindly granted by local landowners. We thank Oliver A. Kern for support with grain-size data presentation. The journal reviewers Louise Hansen and one anonymous person are gratefully acknowledged for their valuable suggestions. Editor-in-Chief Jan A. Piotrowski is thanked for his corrections and the editorial handling. None of the authors has any competing interests. Open Access funding enabled and organized by Projekt DEAL.

Author contributions. – ME: Conceptualization (lead), fieldwork (equal), project administration (equal), methodology (equal), investigation (supporting), writing – original draft (lead), writing – review and editing (equal); KH: Conceptualization (supporting), methodology (equal), investigation (lead), visualisation (lead), writing – original draft (supporting), writing – review and editing (equal); SD: Conceptualization (supporting), fieldwork (equal), writing – review & editing (equal); TP: fieldwork (equal), methodology (equal), writing – review and editing (equal); AK: Methodology (equal), investigation (supporting), writing – review and editing (equal); PV: Methodology (equal), investigation (supporting), writing – review and editing (equal); EK: Methodology (equal), investigation (supporting), writing – review and editing (equal); PK: Fieldwork (equal), methodology (equal), writing – review and editing (equal); IS: Funding acquisition (equal), project administration (equal), writing – review and editing (equal); VMAH: Fieldwork (equal), funding acquisition (equal), project administration (equal), writing – review and editing (equal).

Data availability statement. – Data reported here are stored at heiDA <https://doi.org/10.11588/data/QJEZHT> and are freely accessible under a Creative Commons Attribution 4.0 International Licence (CC BY 4.0) (Hess *et al.* 2023a). Correspondence and requests for materials should be addressed to ME. This study does not use custom code or a mathematical algorithm that is deemed central to the conclusions.

References

- Bahlburg, H. & Weiss, R. 2007: Sedimentology of the December 26, 2004, Sumatra tsunami deposits in eastern India (Tamil Nadu) and Kenya. *International Journal of Earth Sciences* 96, 1195–1209.
- Ballantyne, C. K., Dawson, S., Dick, R., Fabel, D., Kralikaite, E., Milne, F., Sandeman, G. F. & Xu, S. 2018: The coastal landslides of Shetland. *Scottish Geographical Journal* 134, 71–96.
- Bennett, K. D., Boreham, S., Sharp, M. J. & Switsur, V. R. 1992: Holocene history of environment, vegetation and human settlement on Catta Ness, Lunnasting, Shetland. *Journal of Ecology* 80, 241–273.
- Biguenet, M., Sabatier, P., Chaumillon, E., Chagué, C., Arnaud, F., Jorissen, F., Coulombier, T., Geba, E., Cordrie, L., Vacher, P., Deville, A. L., Chalmin, E., Soufi, F. & Feuillet, N. 2021: A 1600-year-long sedimentary record of tsunamis and hurricanes in the Lesser Antilles (Scrub Island, Anguilla). *Sedimentary Geology* 412, 105806, <https://doi.org/10.1016/j.sedgeo.2020.105806>.
- Blaauw, M. & Christen, J. A. 2011: Flexible paleoclimate age–depth models using an auto-regressive gamma process. *Bayesian Analysis* 6, 457–474.
- Blott, S. J. & Pye, K. 2001: GRADISTAT: a grain size distribution and statistics package for the analysis of unconsolidated sediments. *Earth Surface Processes and Landforms* 26, 1237–1248.
- Bondevik, S. 2022: Tsunami from the Storegga Landslide. In Tilling, R. I. (ed.): *Complexity in Tsunamis, Volcanoes, and their Hazards*, 153–185. Springer, Heidelberg.
- Bondevik, S., Mangerud, J., Dawson, S., Dawson, A. G. & Lohne, Ø. 2003: Record-breaking height for 8000 year old tsunami in the North Atlantic. *Eos* 84, 289–293.
- Bondevik, S., Mangerud, J., Dawson, S., Dawson, A. & Lohne, Ø. 2005: Evidence for three North Sea tsunamis at the Shetland Islands between 8000 and 1500 years ago. *Quaternary Science Reviews* 24, 1757–1775.
- Bondevik, S., Stormo, S. K. & Skjerdal, G. 2012: Green mosses date the Storegga tsunami to the chilliest decades of the 8.2 ka cold event. *Quaternary Science Reviews* 45, 1–6.
- Bondevik, S., Svendsen, J. I., Johnsen, G., Mangerud, J. & Kaland, P. E. 1997: The Storegga tsunami along the Norwegian coast, its age and runup. *Boreas* 26, 29–53.
- Brightspec 2015: Technical specifications bAxil Software Package. Available at: <https://www.brightspec.be/brightspec/?q=node/31> (accessed 03.12.2022).
- Buck, L. & Bristow, C. 2020: The relationship between subsurface tsunami features and surface landforms. In Bradford, J. & Comas, X. (eds.): *Proceedings of the 18th International Conference on Ground Penetrating Radar, Golden (CO), USA, 14–19 June 2020*, 267–270. Society of Exploration Geophysicists, Houston.
- Cascalho, J., Costa, P., Dawson, S., Milne, F. & Rocha, A. 2016: Heavy mineral assemblages of the Storegga tsunami deposit. *Sedimentary Geology* 334, 21–33.
- Chagué, C. 2020: Applications of geochemical proxies in paleotsunami research. In Engel, M., Pilarczyk, J., May, S. M., Brill, D. & Garrett, E. (eds.): *Geological Records of Tsunamis and Other Extreme Waves*, 381–401. Elsevier, Amsterdam.
- Chagué-Goff, C., Goff, J., Nichol, S. L., Dudley, W., Zawadzki, A., Bennett, J. W., Mooney, S. D., Fierro, D., Heijnis, H., Dominey-Howes, D. & Courtney, C. 2012: Multi-proxy evidence for trans-Pacific tsunamis in the Hawai'ian Islands. *Marine Geology* 299, 77–89.
- Chapelhow, R. 1965: On glaciation in North Roe, Shetland. *The Geographical Journal* 131, 60–70.
- Chaumillon, E., Bertin, X., Fortunato, A. B., Bajo, M., Schneider, J.-L., Dezileau, L., Walsh, J. P., Michelot, A., Chauveau, E., Créach, A., Hénaff, A., Sauzeau, T., Waeles, B., Gervais, B., Jan, G., Baumann, J., Breilh, J.-F. & Pedreros, R. 2017: Storm-induced marine flooding: lessons from a multidisciplinary approach. *Earth-Science Reviews* 165, 151–184.
- Costa, P. J., Andrade, C., Cascalho, J., Dawson, A. G., Freitas, M. C., Paris, R. & Dawson, S. 2015: Onshore tsunami sediment transport mechanisms inferred from heavy mineral assemblages. *The Holocene* 25, 795–809.
- Costa, P. J. M., Dawson, S., Ramalho, R., Engel, M., Dourado, F., Bosnic, I. & Andrade, C. 2021: A review on onshore tsunami deposits along the Atlantic coasts. *Earth-Science Reviews* 212, 103441, <https://doi.org/10.1016/j.earscirev.2020.103441>.
- Cuven, S., Paris, R., Falvard, S., Miot-Noirault, E., Benbakkar, M., Schneider, J. L. & Billy, I. 2013: High-resolution analysis of a tsunami deposit: case-study from the 1755 Lisbon tsunami in southwestern Spain. *Marine Geology* 337, 98–111.
- Davenport, C. A., Ringrose, P. S., Becker, A., Hancock, P. & Fenton, C. 1989: Geological investigations of late and post glacial earthquake activity in Scotland. In Gregersen, S. & Basham, P. W. (eds.): *Earthquakes at North-Atlantic Passive Margins: Neotectonics and Postglacial Rebound*, 175–194. Springer, Dordrecht.
- Davies, S. J., Lamb, H. F. & Roberts, S. J. 2015: Micro-XRF core scanning in palaeolimnology: recent developments. In Croudace, I. W. & Rothwell, R. G. (eds.): *Micro-XRF Studies of Sediment Cores*, 189–226. Springer, Dordrecht.
- Dawson, A. G. & Shi, S. 2000: Tsunami deposits. *Pure and Applied Geophysics* 157, 875–897.
- Dawson, S., Costa, P., Dawson, A. & Engel, M. 2020a: Onshore archives of tsunami deposits. In Engel, M., Pilarczyk, J., May, S. M., Brill, D. & Garrett, E. G. (eds.): *Geological Records of Tsunamis and Other Extreme Waves*, 95–111. Elsevier, Amsterdam.
- Dawson, A. G., Dawson, S. & Bondevik, S. 2006: A late Holocene tsunami at Basta Voe, Yell, Shetland Islands. *Scottish Geographical Journal* 122, 100–108.
- Dawson, A. G., Dawson, S., Bondevik, S., Costa, P. J., Hill, J. & Stewart, I. 2020b: Reconciling Storegga tsunami sedimentation patterns with modelled wave heights: a discussion from the Shetland Isles field laboratory. *Sedimentology* 67, 1344–1353.
- Dietze, E. & Dietze, M. 2019: Grain-size distribution unmixing using the R package EMMAgeo. *E&G Quaternary Science Journal* 68, 29–46.
- Engel, M., Brückner, H., Messenzehl, K., Frenzel, P., May, S. M., Scheffers, A., Scheffers, S., Wennrich, V. & Kelletat, D. 2012: Shoreline changes and high-energy wave impacts at the leeward coast of Bonaire (Netherlands Antilles). *Earth, Planets and Space* 64, 905–921.
- Engel, M., Oetjen, J., May, S. M. & Brückner, H. 2016: Tsunami deposits of the Caribbean – towards an improved coastal hazard assessment? *Earth-Science Reviews* 163, 260–296.
- Falvard, S. & Paris, R. 2017: X-ray tomography of tsunami deposits: towards a new depositional model of tsunami deposits. *Sedimentology* 64, 453–477.
- Flinn, D. 1964: Coastal and submarine features around the Shetland Islands. *Proceedings of the Geologists' Association* 75, 321–339.
- Flinn, D. 1974: The coastline of Shetland. In Nature Conservation Council (ed.): (ed.): *The Natural Environment of Shetland. Proceedings of the Nature Conservancy Council Symposium, 29–30 January 1974*, 13–23. Nature Conservation Council, Edinburgh.
- Folk, R. L. & Ward, W. C. 1957: Brazos River bar [Texas]; a study in the significance of grain size parameters. *Journal of Sedimentary Research* 27, 3–26.
- Gillen, C. 2003: *Geology and Landscapes of Scotland*. 256 pp. Terra, Harpenden.
- González, F. I. and 20 others 2009: Probabilistic tsunami hazard assessment at Seaside, Oregon, for near- and far-field seismic sources. *Journal of Geophysical Research* 114, C11023, <https://doi.org/10.1029/2008JC005132>.
- Goslar, T., Czernik, J. & Goslar, E. 2004: Low-energy ¹⁴C-AMS in Poznań Radiocarbon Laboratory, Poland. *Nuclear Instruments and Methods in Physics Research Section B: Beam Interactions with Materials and Atoms* 223–224, 5–11.
- Haflidason, H., Lien, R., Sejrup, H. P., Forsberg, C. F. & Bryn, P. 2005: The dating and morphology of the Storegga slide. *Marine and Petroleum Geology* 22, 123–136.
- Halliday, R. 2011: Shetland Islands – Wave and tidal resource. *Shetland Islands Council Report 805_NPC_SIC_R_004*. Available at: <https://www.shetland.gov.uk/downloads/file/1870/wave-and-tidal-resource> (accessed 08.08.2023).
- Hess, K., Engel, M. & Koutsodendris, A. 2023a: Sedimentological storm and tsunami record of Loch Flugarth, Shetland Islands (UK). *heidata*, <https://doi.org/10.11588/data/QJEZHT>.

- Hess, K., Engel, M., Patel, T., Vakhrameeva, P., Koutsodendris, A., Klemm, E., Hansteen, T. H., Kempf, P., Dawson, S., Schön, I. & Heyvaert, V. M. A. 2023b: A 1500-years record of North Atlantic storm flooding from lacustrine sediments, Shetland Islands (UK). *Journal of Quaternary Science*, <https://doi.org/10.1002/jqs.3568>.
- Hoppe, G., Fries, M. & Quennerstedt, N. 1965: Submarine peat in the Shetland Islands. *Geografiska Annaler* 47A, 195–203.
- Kassambara, A. 2017: *Practical Guide to Principal Component Methods in R (Multivariate Analysis Book 2)*. 170 pp. STHDA, Marseille.
- Kelsey, H. M., Nelson, A. R., Hemphill-Haley, E. & Witter, R. C. 2005: Tsunami history of an Oregon coastal lake reveals a 4600 yr record of great earthquakes on the Cascadia subduction zone. *Geological Society of America Bulletin* 117, 1009–1032.
- Kempf, P., Moernaut, J., Van Daele, M., Vandoorne, W., Pino, M., Urrutia, R. & De Batist, M. 2017: Coastal lake sediments reveal 5500 years of tsunami history in south central Chile. *Quaternary Science Reviews* 161, 99–116.
- Kempf, P., Moernaut, J., Van Daele, M., Vermassen, F., Vandoorne, W., Pino, M., Urrutia, R., Schmidt, S., Garrett, E. & De Batist, M. 2015: The sedimentary record of the 1960 tsunami in two coastal lakes on Isla de Chiloe, south central Chile. *Sedimentary Geology* 328, 73–86.
- Kern, O. A., Koutsodendris, A., Mächtle, B., Christanis, K., Schukraft, G., Scholz, C., Kotthoff, U. & Pross, J. 2019: XRF core scanning yields reliable semiquantitative data on the elemental composition of highly organic-rich sediments: evidence from the Fürmoos peat bog (Southern Germany). *Science of the Total Environment* 697, 134110, <https://doi.org/10.1016/j.scitotenv.2019.134110>.
- Kylander, M. E., Söderlindh, J., Schenk, F., Gyllencreutz, R., Rydberg, J., Bindler, R., Martínez Cortizas, A. & Skelton, A. 2020: It's in your glass: a history of sea level and storminess from the Laphroaig bog, Islay (southwestern Scotland). *Boreas* 49, 152–167.
- Liu, K.-B. 2004: Palaeotempestology: principles, methods, and examples from Gulf Coast lake sediments. In Murname, R. J. & Liu, K.-B. (eds.): *Hurricanes and Typhoons: Past, Present and Future*, 13–57. Columbia University Press, New York.
- Long, D. 2015: A catalogue of tsunamis reported in the UK. *British Geological Survey Internal Report IR15/043*. Available at: <http://nora.nerc.ac.uk/id/eprint/513298> (accessed 03.12.2022).
- Mac Conamhna, O. A. P. 2023: A seismic tsunami in the Irish annals, recorded at Iona in October 720. *Marine Geology* 456, 106973, <https://doi.org/10.1016/j.margeo.2022.106973>.
- McIlvenny, J. D., Muller, F. & Dawson, A. 2013: A 7600-year sedimentary record of climatic instability in Dunnet Bay, North Scotland. *Marine Geology* 335, 100–113.
- Moore, A., Goff, J., McAdoo, B. G., Fritz, H. M., Gusman, A., Kalligeris, N., Kalsum, K., Susanto, A., Suteja, D. & Synolakis, C. E. 2011: Sedimentary deposits from the 17 July 2006 western Java tsunami, Indonesia: use of grain size analyses to assess tsunami flow depth, speed, and traction carpet characteristics. *Pure and Applied Geophysics* 168, 1951–1961.
- Murray, J. & Pullar, L. 1908: Bathymetric map, Loch of Flugarth; Eela Water. In Murray, J. & Pullar, L. (eds.): *Bathymetrical Survey of the Freshwater Lochs of Scotland*, Vol. 6, Plate 99. Royal Geographical Society, London.
- Musson, R. M. W. 2007: British earthquakes. *Proceedings of the Geologists' Association* 118, 305–337.
- Mykura, W., Flinn, D. & May, F. 1976: *British Regional Geology – Orkney and Shetland*. 149 pp. National Environment Research Council, Institute of Geological Sciences, Edinburgh.
- Piccardi, L. 2014: Post-glacial activity and earthquakes of the Great Glen Fault (Scotland). *Memorie Descrittive della Carta Geologica d'Italia XCVI*, 431–446.
- Pringle, I. R. 1970: The structural geology of the North Roe area of Shetland. *Geological Journal* 7, 147–170.
- Reimer, P. J. and 41 others 2020: The IntCal20 Northern Hemisphere radiocarbon age calibration curve (0–55 cal kBP). *Radiocarbon* 62, 725–757.
- Ringrose, P. S. 1989: Recent fault movement and palaeoseismicity in western Scotland. *Tectonophysics* 163, 305–314.
- Romundset, A., Fredin, O. & Høgaas, F. 2015: A Holocene sea-level curve and revised isobase map, S Norway. *Boreas* 44, 383–400.
- Sabatier, P., Moernaut, J., Bertrand, S., Van Daele, M., Kremer, K., Chaumillon, E. & Arnaud, F. A. 2022: Review of event deposits in lake sediments. *Quaternary* 5, 34, <https://doi.org/10.3390/quat5030034>.
- Schillereff, D. N., Chiverrell, R. C., Macdonald, N. & Hooke, J. M. 2014: Flood stratigraphies in lake sediments: a review. *Earth-Science Reviews* 135, 17–37.
- Schindelin, J., Arganda-Carreras, I., Frise, E., Kaynig, V., Longair, M., Pietzsch, T., Preibisch, S., Rueden, C., Saalfeld, S., Schmid, B., Tinevez, J.-Y., White, D. J., Hartenstein, V., Eliceiri, K., Tomancak, P. & Cardona, A. 2012: Fiji: an open-source platform for biological-image analysis. *Nature Methods* 9, 676–682.
- Smith, D. E. 1993: Norwick, Unst; Burragarth, Unst; Sullom Voe, Mainland. In Birnie, J., Gordon, J., Bennett, K. & Hall, A. M. (eds.): *The Quaternary of Shetland*, 52–56. Quaternary Research Association, London.
- Smith, D. E., Barlow, N. L. M., Bradley, S. L., Firth, C. R., Hall, A. M., Jordan, J. T. & Long, D. 2019: Quaternary sea level change in Scotland. *Earth and Environmental Science Transactions of the Royal Society of Edinburgh* 110, 219–256.
- Smith, D. E., Shi, S., Cullingford, R. A., Dawson, A. G., Dawson, S., Firth, C. R., Foster, I. D. L., Fretwell, P. T., Haggart, B. A., Holloway, L. K. & Long, D. 2004: The Holocene Storegga Slide tsunami in the United Kingdom. *Quaternary Science Reviews* 23, 2291–2321.
- Sohn, Y. K. 1997: On traction-carpet sedimentation. *Journal of Sedimentary Research* 67, 502–509.
- Spiske, M. 2020: The sedimentology and geometry of fine-grained tsunami deposits in onshore environments. In Engel, M., Pilarczyk, J., May, S. M., Brill, D. & Garrett, E. (eds.): *Geological Records of Tsunamis and Other Extreme Waves*, 213–238. Elsevier, Amsterdam.
- Stuiver, M. & Reimer, P. J. 1993: Extended ¹⁴C data base and revised CALIB 3.0 ¹⁴C age calibration program. *Radiocarbon* 35, 215–230.
- Swindles, G. T., Galloway, J. M., Macumber, A. L., Croudace, I. W., Emery, A. R., Woulds, C., Bateman, M. D., Parry, L., Jones, J. M., Selby, K., Rushby, G. T., Baird, A. J., Woodroffe, S. A. & Barlow, N. L. M. 2018: Sedimentary records of coastal storm surges: evidence of the 1953 North Sea event. *Marine Geology* 403, 262–270.
- Switzer, A. D. & Jones, B. G. 2008: Large-scale washover sedimentation in a freshwater lagoon from the southeast Australian coast: sea-level change, tsunami or exceptionally large storm? *The Holocene* 18, 787–803.
- Szczuciński, W. 2020: Post-depositional changes to tsunami deposits and their preservation potential. In Engel, M., Pilarczyk, J., May, S. M., Brill, D. & Garrett, E. (eds.): *Geological Records of Tsunamis and Other Extreme Waves*, 443–468. Elsevier, Amsterdam.
- Wagner, B., Bennike, O., Klug, M. & Cremer, H. 2007: First indication of Storegga tsunami deposits from East Greenland. *Journal of Quaternary Science* 22, 321–325.
- Wahl, T., Haigh, I. D., Woodworth, P. L., Albrecht, F., Dillingh, D., Jensen, J., Nicholls, R. J., Weisse, R. & Wöppelmann, G. 2013: Observed mean sea level changes around the North Sea coastline from 1800 to present. *Earth-Science Reviews* 124, 51–67.
- Weiss, R. & Bourgeois, J. 2012: Understanding sediments – reducing tsunami risk. *Science* 336, 1117–1118.

Supporting Information

Additional Supporting Information to this article is available at <http://www.boreas.dk>.

Data S1. The chronostratigraphy at Flugarth (see also Hess et al. 2023b).

Fig. S1. View from northeast towards southwest to the coastline of Sand Voe beach and Loch Flugarth. Left: Erosional features indicate a high erosional wave dynamic during storms (photograph modified from Colin Smith, (geograph 2 076 880), CC BY-SA 2.0).

Fig. S2. A. The zodiac used for sampling moored on the eastern shore of Loch Flugarth. B. UWITEC gravity corer used for the extraction of FLUG 2–4 (photographs by T. Patel).

Fig. S3. Overview of the lithostratigraphy. From left to right: light photograph and CT scan of FLUG 2; light photograph, CT scan and facies distribution of FLUG 3, including key correlation layers with FLUG 2; high-resolution data of Fe/Ti and Sr/Rb ratios, and Sr/Br ratios, respectively (modified from Hess *et al.* 2023b). The red box indicates the core section shown in Fig. 5. The time scale refers to core FLUG 3.

Fig. S4. Photograph and field log of sediment core FLUG 1, taken with a Russian chamber corer at 200–250 cm below lake bottom (b.s.) (Fig. 1D, main text). Even though FLUG 2 and FLUG 3 did not reach below the base of the candidate tsunami deposit, FLUG 1 unequivocally shows the lacustrine facies of presumably Holocene age underneath.

Fig. S5. PCA of centred log-ratio transformed elements.

Fig. S6. Biplot showing the results of the principal component analysis (PCA). Numbers indicate the depths of a measurement in centimetres b.s. The variables (element ratios) of the PCA are represented by arrows. The length of the arrows indicates the representativeness of each variable in relation to the first two dimensions.

Fig. S7. A. Scree plot showing the percentage of the explained variance per dimension/principal component. B. Quality of representation (cos²) of each variable (proxies) in each dimension.

Fig. S8. Detailed depictions of small rip-up clasts in sublayers 2–4 of the candidate tsunami deposit. A. CT scan in planar view of FLUG 3 at a depth of ~79.5 cm b.s. (sublayer 4) showing an almost round rip-up clast of peat floating in the sandy matrix. B. Several very small rip-up clasts with varying shapes. The largest one is found in the upper part of the normally graded subsequence of sublayer 2. It has an irregular shape and its longest axis has a vertical orientation. Small millimetre-scale peat clasts are distributed in sublayers 3 and 4.

Table S1. Results of the mathematical ¹³⁷Cs modelling (Hess *et al.* 2023b). b.s. = below surface.

Table S2. The 19 most pronounced event deposits that were included and considered in the age–depth model with their calculated ages (Hess *et al.* 2023b).

Table S3. ¹⁴C data of relevant samples from stratigraphic sections at Basta Voe (BV) and Dury Voe (DV) containing tsunami deposits of the Dury Voe event. The data and sample information were taken from Bondevik *et al.* (2005) and recalibrated using the most recent IntCal20 calibration curve (Reimer *et al.* 2020).